Application of a hybrid pixel detector to powder diffraction

S. Basolo,[a] J.-F. Bérar,[b,c]* N. Boudet,[b,c] P. Breugnon,[a] B. Caillot,[b,c]
J.-C. Clemens,[a] P. Delpierre,[a] B. Dinkespiler,[a] S. Hustache,[d] I. Koudobine,[a]
Ch. Meessen,[a] M. Menouni,[a] C. Mouget,[c] H. Palancher,[c] P. Pangaud,[a]
R. Potheau[a] and E. Vigeolas[a]

[a]CPPM-IN2P3, Luminy, 13288 Marseille, France, [b]D2AM-CRG/F, ESRF, 38043 Grenoble, France,
[c]Institut Néel, CNRS, 38042 Grenoble, France, and [d]Synchrotron SOLEIL, Saint-Aubin, 91192 Gif
sur Yvette, France. E-mail: berar@esrf.fr

Results obtained using a hybrid pixel photon-counting detector in powder diffraction experiments are presented. The detector works at room temperature and its dynamic response ranges from 0.01 photons $pixel^{-1} s^{-1}$ up to 10^6 photons $pixel^{-1} s^{-1}$. The pixel sizes are 0.33 mm $\times$ 0.33 mm for a total area of 68 mm $\times$ 68 mm. On recording high-resolution diffraction patterns of powders, a reduction of the experimental time by more than a factor of 20 is obtained without loss of data quality. The example of an X-zeolite shows that such detectors can be used for very demanding anomalous experiments. *In situ* experiments of quenching liquid oxides show that frames of 0.01 s can be achieved for studying such processes.

1. Introduction

Many present-day experiments are still performed using slits and point detectors (scintillators associated with photo-multipliers) because they require either high dynamics, low noise or fast readout. In high-resolution synchrotron radiation experiments using analyser crystals, this situation always seems to be the case. However, other arrangements may also be used. For instance, linear detectors can be found in experiments requiring short acquisition times.

In the 1990s the two-dimensional detectors available were image plates characterized by long readout times and persistence of the most intense spots. Later, two-dimensional CCDs combined with a phosphor screen appeared on the market and replaced the image plates. These, however, also have disadvantages. They have a small dynamic range and their readout time is too long for time-resolved experiments such as irreversible phase transitions or metastable phase characterization. Another drawback of such two-dimensional cameras is their high background noise at room temperature, and for this reason CCDs are cooled. Furthermore, their pixel size is small compared with the X-ray source size and they often require optical demagnification using phosphor screens. These multiple stages corrupt the transfer function and the statistical properties of the counting can be lost. Several attempts are now being made to develop photon-counting devices with a fast readout (Eikenberry *et al.*, 1998). Among the choices are hybrid pixel detectors operating at room temperature and based on semiconductor diode sensors connected to dedicated front-end electronic chips using bump and flip-chip technology. Depending on the application, different choices can be made for the design of the electronics, pixel size and type of sensor. Different projects have been developed in response to the increasingly demanding requirements of protein crystallography (Brönnimann *et al.*, 2000) as well as medical imaging (Watt *et al.*, 2001). In our case, we are interested in more general crystallographic applications, such as the measurement of diffuse scattering and small-angle X-ray scattering, for which the precise asymptotic behaviour is investigated. In both cases, low count rates are encountered and, to minimize the noise introduced by background subtraction, the dark counts of the detector must also be very low. Results of the Pilatus project have been recently published concerning the application of such pixel detectors to grazing-incidence experiments in materials science (Schlepütz *et al.*, 2005).

In this paper we report results obtained using an improved prototype of the photon-counting detector (Basolo *et al.*, 2005) using XPAD2 chips for powder diffraction experiments. The whole detector, which is composed of eight modules of eight chips each, incorporates 38400 hybrid pixels. Unlike dedicated one-dimensional detectors, such as the RAPID gas detector of the SRS or the microstrip PSI detector, the XPAD2 detector is a two-dimensional pixel detector which does not directly supply one-dimensional data. It yields anisotropic images but, owing to its size (200 $\times$ 192 pixels), the XPAD2 detector must be moved if high-resolution data are to be recorded. By

151

contrast, the MYTHEN one-dimensional PSI detector covers an angular range of 60° in 15000 steps. In principle, although one-dimensional data can be extracted from two-dimensional images, they frequently do not achieve the expected one-dimensional data quality that is mandatory for high-resolution Rietveld refinements. With the present detector this difficulty has been overcome and advantage can be taken of its wide axial aperture to improve the counting statistics.

2. The 8 module prototype detector

In our detector (Delpierre *et al.*, 2001, 2002; Bérar *et al.*, 2002*a*,*b*), incoming absorbed photons are converted into an electron cloud in the sensor in which an electric field ensures migration of the charges towards the bump to the electronic chip. In each pixel the electron bunches are then treated by dedicated electronics, consisting of a pre-amplifier, a shaper, a discriminator and a counter. By virtue of the wide parallel structure, very short reading times can be achieved (less than 1 ms).

The design of the XPAD2 prototypes is based on the first-generation XPAD1; the chips were manufactured by AMS with 0.8 μm CMOS technology.

Owing to the observed broad distribution of threshold levels within XPAD1 chips, parts of the design were modified to reduce this dispersion. At the same time the associated electronics were redesigned to conform with the project requirements. As the electronic characteristics of the XPAD2 chips have already been reported (Boudet *et al.*, 2003), this paper recalls some of the characteristics of the large area detector.

The chips are bump-bonded to new 0.50 mm-thick Si diodes. Each diode is associated with eight chips of 24×25 pixels. This unified assembly appears as an independent module for the output electronics, and is wire-bonded to a small PCB card (class 6) on which are mounted a few electronic line drivers and a voltage regulator (Fig. 1). All modules are independently connected through low-insertion-force 225×25-way connectors to the acquisition card, which is based on an Alterra Nios development module and allows
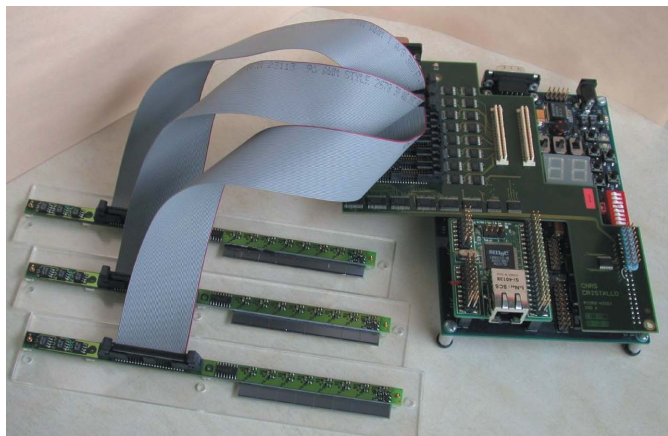

Figure 1
Three detector modules wired to an acquisition card.

Figure 2
The 8 module detector plate viewed from its connector side.

direct Ethernet communication with the detector. This parallelism allows the dead-time between two images to be reduced to a few ms.

In building the new detector (Basolo *et al.*, 2005), eight of these modules are assembled together (Fig. 2) and tiled as close as possible to each other to reduce shading and dead zones. They are positioned on a metallic holder with an accuracy of a few micrometres. The detector size is 200 pixels $\times$ 192 pixels. Note that in each module of eight chips the diodes provide a continuous detection area.

3. From multiple XPAD images to Debye–Scherrer high-resolution data

High-quality diffraction data sets needed for Rietveld refinement of complex structures are characterized by a small angular step and a wide angular range. This leads to typical steps smaller than 0.01° and records intensities at more than 10000 regularly spaced angular positions. In recent synchrotron diffractometer experiments this is often performed in a continuous scan with a bank of detectors. However, since some of these experiments do not require an analyser crystal, it seems possible to use images collected by the XPAD to obtain such data.

3.1. Experimental arrangement

To preserve the angular resolution, which in this arrangement is limited by the beam size and not by the pixel size, the XPAD detector is fixed at the same distance from the sample as the slits and the scintillator detector on the diffractometer arm. In this configuration the XPAD collects data from an area about 200×10 bigger, which compensates for the lower efficiency of the diodes: 60% at 16 keV, 38% at 20 keV. The gain in surface area also compensates for the significant number of imperfectly tuned pixels.

As an example, the diffraction pattern from a simple powder (CeO_2 from NIST) was recorded at 20 keV in standard reflection geometry, on the goniometer of the D2AM CRG beamline at the ESRF, with the detector located at 1 m from the sample. At this distance the total angular aperture is almost 4° and the pixel size is 0.02°. The first ($2\theta = 18°$) and the last images are shown in Fig. 3. Each image was recorded for
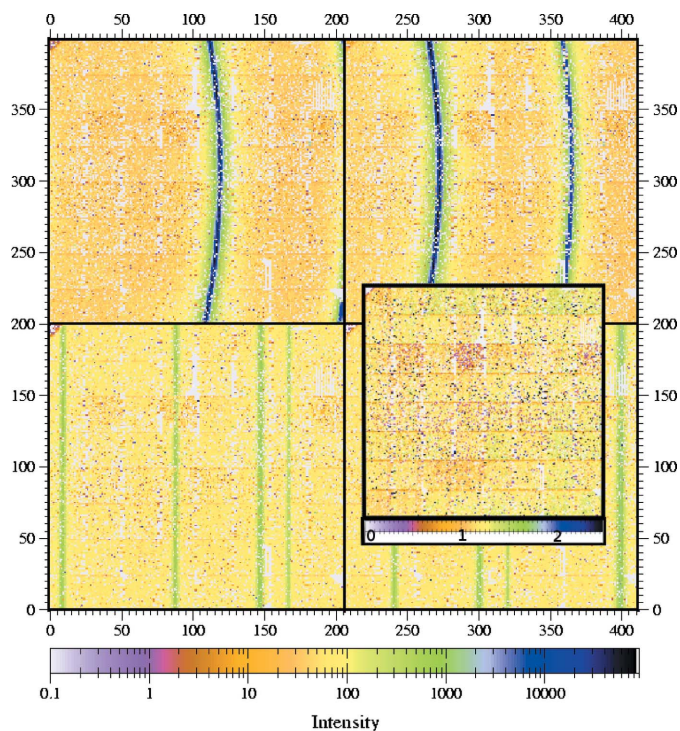
Figure 3
The two first and last images of the CeO$_2$ XPAD collection (1° per step) on a log scale. Insert: detector flat field extracted from the data collection.

5 s using an angular step of 1.0° in 2θ. Each Bragg line was recorded three or four times, thus yielding considerable data redundancy. The data collection time was less than 10 min, which is 100 times shorter than the 3–8 h used for a conventional experiment with a step size of 0.01°. The redundancy in our data allows the effective flat field of the detector to be extracted during this experiment (see insert in Fig. 3).

The advantage of this data collection strategy is that a pattern is not obtained directly but a set of images that allows both a simple linear 2θ data set and a Debye–Scherrer cylindrical film to be constructed in which the preferred orientation and any 'graininess' in the sample can be revealed. It is therefore quicker and, in a given measuring time, more information is obtained.

3.2. From images to data set

We first recall that it is difficult to obtain a flat field with the necessary accuracy at the energy used for each experiment. Since the flat field must be recorded for the energy of the incident photons, a fluorescent sample cannot be used as it yields a complex energy spectrum. The best way appeared to be to record the diffuse elastic response of a 'flat' scatterer such as water at each experimental energy. Since the scattering power is low, however, long exposures are needed to reach the desired statistical accuracy. Moreover, the real shape of such experimental flat fields is not easy to model and redundancy in the image is necessary to extract the flat-field correction coefficients. In a powder experiment, where similar redundancy arises, the data collection was performed by tuning the

detector in this energy range and recording all pixels. The diffraction pattern is then constructed from the experimental data.

The counts obtained in a resulting element of the reconstructed diffraction pattern (a 2θ step for linear patterns, a pixel in the case of cylindrical Debye–Scherrer films) are the weighted sum of the valid counts from all pixels in all images giving a contribution in this element. However, raw counts must be corrected for flat-field distortion and geometrical errors. This yields, for the resulting Y counts on element p,

$$Y_p = N_p^{-1} \sum_i^{\text{images}} \sum_q^{\text{pixels}} \omega_{q,i}\, \sigma_{q,i}(p)\, \gamma_{q,i}\, y_{q,i}\, \varphi_q, \qquad (1)$$

where $y_{q,i}$ are counts on image i of pixel q, φ_q is the flat field for pixel q, $\omega_{q,i}$ is the weight of pixel q in image i (= 1 if counts are valid, 0 elsewhere), $\sigma_{q,i}(p)$ is the projection of pixel q in image i on the element p along the diffracted beam, $\gamma_{q,i}$ is the geometrical correction factor for pixel q in image i and $N_p = \Sigma_i \Sigma_q \omega_{q,i} \sigma_{q,i}(p)$ is the normalizing factor.

In the above expression the surface projection $\sigma_{q,i}(p)$ is zero for most of the pixels. In powder linear patterns it takes a non-negligible value only for the pixels on the diffraction cone associated with 2θ equal to $2\theta_p$. In the case of a cylindrical Debye–Scherrer film, this projection exists only for the few corresponding pixels of the image.

Expression (1) does not assume any particular configuration and readily allows for the real experimental geometry. The projection $\sigma_{q,i}(p)$ takes account of the position of the detector (zero in 2θ), its misalignment (e.g. rotation around the beam) and also the real geometry of the pixels inside the detector.

For an ideal powder with no preferred orientation, where a flat distribution of the intensities is expected, the product $\gamma_{q,i}\, y_{q,i}\, \varphi_q$ should be constant and equal to Y_p. When the flat field is known, (1) gives directly the expected result and its statistical dispersion. The standard deviation can obviously be obtained from the experimental dispersion of $y_{q,i}$. The first raw results can then be improved by removing excessively noisy counts in the measurement with a known confidence level.

When the flat field is unknown, the data can also be extracted if there is enough redundancy in the measurements. In this case the expected result is also obtained from (1), but using an iterative procedure starting with a uniform flat field ($\forall q \; \varphi_q = 1$). To ensure convergence of the procedure, it may be useful to exclude the worst pixels before starting. Flat-field values are obtained by minimizing the differences between Y_p and $\gamma_{q,i}\, y_{q,i}\, \varphi_q$ for all pixels q,i participating in the element p [$\sigma_{q,i}(p) > 0$]. Then the process is iterated a few times. Although a complete standard least-squares minimization process may be employed, the method used simultaneously allows badly tuned pixels to be inspected and removed. An example of such a flat field is displayed as an insert in Fig. 3. The original 10% of badly tuned pixels (including 3% dead pixels) were increased to approximately 20% to meet the requirement of a homogeneous flat field on which can be seen the horizontal lines associated with the boundary pixels of each module that partially overlap their neighbours.
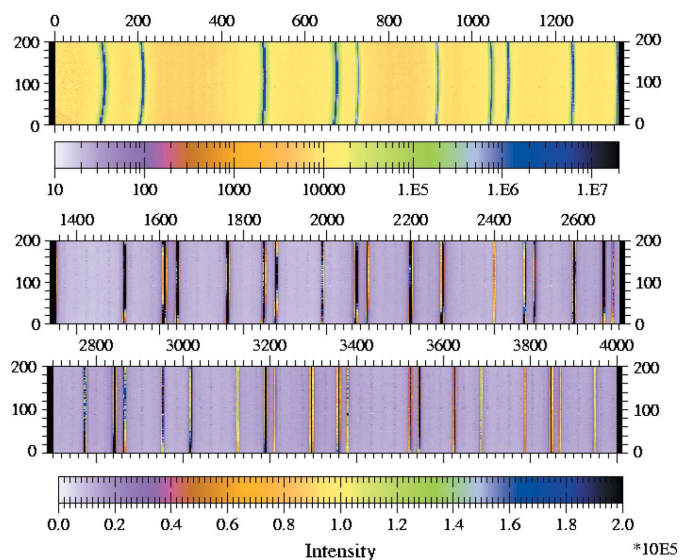
Figure 4
Debye–Scherrer reconstructed film from (1° per step) data.

This calculation is carried out using scripts written in *Python* (PSF, 2006), which use tables of the pixels q,i used for element p instead of $\omega_{q,i}(p)$. Data can be processed according to (1) to construct a Debye–Scherrer film which allows preferred orientations in the sample or effects of grain statistics to be revealed that are not directly discernible in a linear plot. The film from the CeO_2 sample is shown in Fig. 4. Using 2θ steps of 1°, the Debye–Scherrer film shows information over the whole angular domain. At small angles the diffraction cone exhibits a curvature on the line that is not present at $2\theta = 90°$.

3.3. The X-zeolite sample

The technique described in the previous section was employed to obtain high-resolution data on an X-zeolite sample. Data were recorded on the ESRF BM2 beamline using a dedicated reaction cell in which the sample lies in an oscillating ($\pm55°$) open capillary that permits gas flow (Palancher, Pichon *et al.*, 2005). Conventional data were acquired without the analyser crystal, but by using slits with similar conditions; the angular aperture of the slits (0.020°) was chosen to fit the direct beam width on the sample. The observed line-width was close to 0.035° and the equatorial aperture of the detector slit was set to preserve the line profile quality. A measurement time of 2 s was chosen to maintain the statistical average due to the sample oscillation period associated with the gas line. Detailed structural results obtained from a bicationic X-zeolite with such an arrangement have recently been published (Palancher, 2004; Palancher, Hodeau *et al.*, 2005; Palancher *et al.*, 2006).

To allow comparison of the data, the same incoming setting was used with the XPAD detector. The receiving slits and scintillation counter were simply replaced by the XPAD. A tube used to eliminate diffuse scattering was also removed. Table 1 lists both experimental settings. With the measurement time for each step being fixed by the oscillating sample, the increase in the collecting area was used to reduce the number

Table 1
Experimental conditions for recording conventional and XPAD data on the X-zeolite.

	Slits	XPAD
Beam energy	16.097 keV	16.097 keV
Beam slits	0.7 mm × 1 mm	0.7 mm × 1 mm
Sample–detector distance	1 m	1 m
Slits/pixel height	0.35 mm (slits)	0.330 mm (pixel)
Equatorial aperture	10 mm (slits)	64 mm (detector)
Detector efficiency	~99%	40%
Recorded step number	9000	600
Recorded step width	0.006°	0.1°
Counting time	2 s per step	2 s per step
Acquisition time	~6 h 30 min	~0 h 25 min
Data step number	8668	5151
Data step width	0.006°	0.01°
Data range (2θ)	2–54°	2.6–54.1°
FWHM at 10, 20, 30°	0.035, 0.042, 0.054°	0.043, 0.045, 0.054°

of measurement steps. The acquisition time, taking into account motion, was divided by 16 as no extra dead-time is introduced by reading the XPAD image. The improvement of the collecting area largely offsets the lower quantum efficiency of silicon: the direct sum of the counts at a given Bragg angle on each image is expected to be 2.5 times higher than with the conventional arrangement, and, although 10% of the pixels are not usable, the gain on each image still prevails. By recording the XPAD image with 0.1° steps the same Bragg line is measured ~40 times, since the whole angular aperture of the detector was 3.9° in 2θ. Thus, for similar conditions, the total number of counts for one angular step is expected to be ~100 times greater than with the conventional arrangement. The observed standard deviation estimated from fluctuations between images or between points seems, however, not to be reduced by ~10. This could be related to dispersion in extracting the flat field from (1).

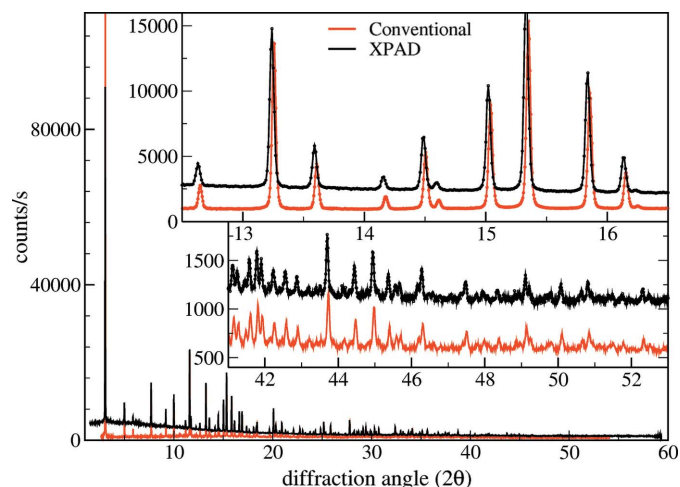The data from the hydrated CaSrX-zeolite are represented in Fig. 5 together with those obtained with the conventional

Figure 5
XPAD data (0.1° per step) of a CaSrX-zeolite compared with conventional (slits) at 16.097 keV. All other experimental parameters are similar. XPAD data have been scaled to exhibit similar line intensities above background at high angles. Inserts are zoomed parts of the diagrams.

method. The values calculated according to equation (1) are displayed in steps of 0.01° and are scaled to exhibit similar counts above the background at wide angles. The scattering at small angles is associated with air scattering and cannot be avoided using two-dimensional detectors. At wide angles, where the signal is weak, the XPAD data are of very good quality and better than from the conventional technique, although the background is higher. This change in background can be explained by a wider integration of whole scattering from the sample and the environment.

The line widths observed with the XPAD are slightly larger than those observed using the conventional system. This is more significant in the low-angle region where the width obtained after processing is strongly dependent on the exact geometrical description of the pixels in the experiment. This width is also related to the step size used in processing (1), which appears to have a convoluting width; data have been processed with a step of 0.01°, approximately half of the pixel size. This will be improved in the future as XPAD3 pixels will be smaller. The XPAD profiles were taken as pseudo-Voigt (0.15) in *FullProf* (Rodriguez-Carvajal, 2001) and the asymmetry parameters remain low.

To ensure the quality of the data, a Rietveld refinement of the zeolite (Fig. 6) was achieved. For both experimental methods all refined structural parameters are in quantitative agreement. A difference between the two refinements is found only in the isotropic thermal factor of the network oxygen, 2.31 Å for the conventional data, whereas it is 2.77 (5) Å^2 for the XPAD. The residual factors (Table 2) are equivalent to those obtained using conventional data. In both cases more than 90% of the points are contributing to Bragg lines. A χ^2 value of 3.3 was obtained, but this value has to be considered together with the scaling factor applied to Y obtained by (1); at the time, the weighting scheme deduced directly from the sum (1) was not satisfactory and conventional weights have been used in these scaled data. It is therefore possible to record high-quality data using XPAD in 1/20 of the time. This
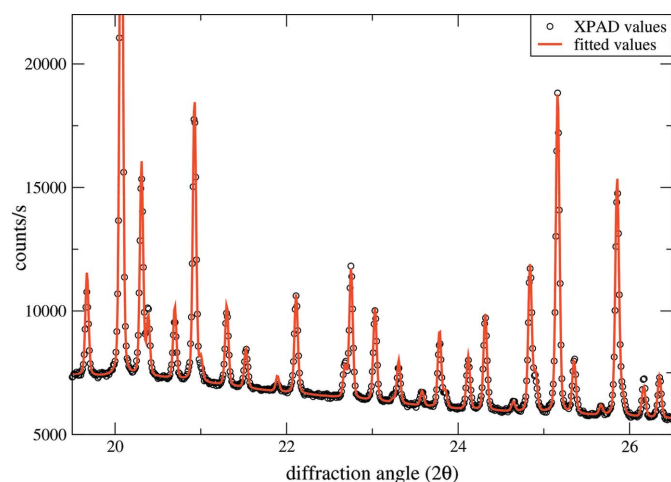
Table 2
Summary of Rietveld refinement for conventional and XPAD data on the X-zeolite at 16.097 keV.

	Slits	XPAD
Conventional Rietveld Residuals	R_p = 7.6% R_{wp} = 6.2% R_{exp} = 3.0% R_{Bragg} = 2.5%	R_p = 9.5% R_{wp} = 6.8% R_{exp} = 3.7% R_{Bragg} = 2.5%

reduces the experimental time at each temperature from more than 6 h to about half an hour, taking into account goniometer motor motions.

3.4. Anomalous experiments

In complex zeolites, anomalous diffraction is the ideal method for locating the exchanged cations, even in bicationic systems. The small difference in the structure factors allows the occupancy of disordered insertion sites to be checked. However, this kind of study requires data of very high quality to ensure that the small deviations in the signal are significant. The CaSrX-zeolite pattern was recorded near to (16.097 keV) and far from (15.192 keV) the Sr edges. They are represented in Fig. 7(*a*), the abscissa being expressed in $1/d$ to allow direct comparison of the peaks. The data measured near the Sr edge have a slightly higher background due to the fluorescence.

The quality of this difference signal is similar to that obtained with the standard detection set-up (Palancher, Hodeau *et al.*, 2005) but data were recorded in 1/16 of the time. The structural model for the zeolite was also refined using these data, which allow the insertion sites occupied by the Sr ions to be distinguished from those occupied by water molecules and Ca^{2+} cations, just as with conventional data sets. The difference signal, centred on 0 after intensity normalization, shows that some peaks depend on the anomalous effect. A Fourier difference map obtained from these data is shown in Fig. 7(*b*); the Sr insertion site is well located.

4. Kinetics measurements

The parallel architecture used throughout the detector design favours real-time measurements. On-board memories allow storage of several frames for such experiments on kinetics: 423 images with less than 10 ms exposure (16 bits) or 233 images exposed for more than 10 ms (32 bits). In both cases the dead-time between two consecutive images is no more than 2 ms. The full movie is transferred afterwards to the acquisition PC after the measurement *via* a 100 MB ethernet link. To illustrate the potential of this detector, we recorded the quenching of refractive oxides from their liquid state. In these experiments the conventional set-up does not allow data to be recorded sufficiently fast to follow the quench. Depending on the conditions, crystallized or amorphous samples can be obtained and an intermediate phase appears. For this reason a linear gas detector is used, but to avoid detector saturation the direct beam intensity must be attenuated, to the detriment of the counting statistics.
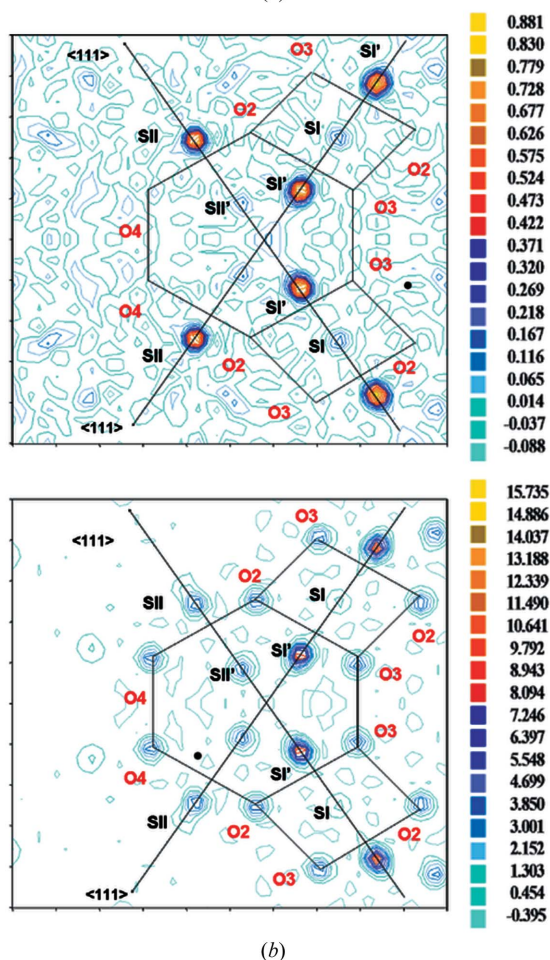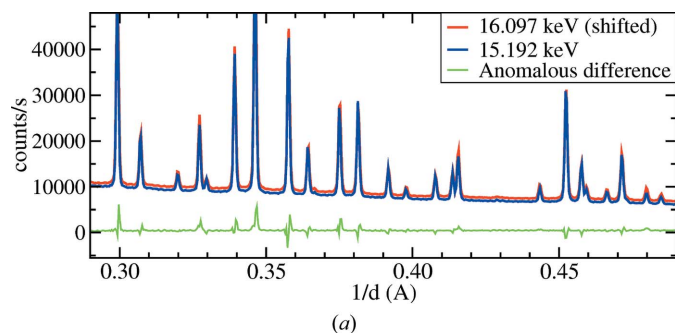

Figure 6
Rietveld fit of XPAD experimental data of the CaSrX-zeolite at 16.097 keV. This zoom allows comparison of the experimental (circles) with the fitted (line) data.

Figure 7
(*a*) Anomalous diffraction pattern of the zeolite showing the effect of ionic substitution as recorded with the XPAD pixel detector. (*b*) Two Fourier maps of the same plane [defined by two (111) axes]: the anomalous map of the difference map (top) obtained with these data allows the inserted Sr cations to be located. These sites are mainly sites I′ and II of the standard electron density map (bottom) in which the framework is displayed.

The experimental cell used here was designed for a conventional experiment on molten levitated oxides (Hennet *et al.*, 2003*a*,*b*) and the horizontal aperture was restricted to 5 mm. This did not take full advantage of the area of the XPAD since only two modules were illuminated by the scattered beam. A laser heated a small $CaO.2Al_2O_3$ sphere above its melting point; then the laser power was switched off and XPAD data were recorded during the quench. A full movie of 223 images of 20 ms separated by a dead-time of 2 ms was
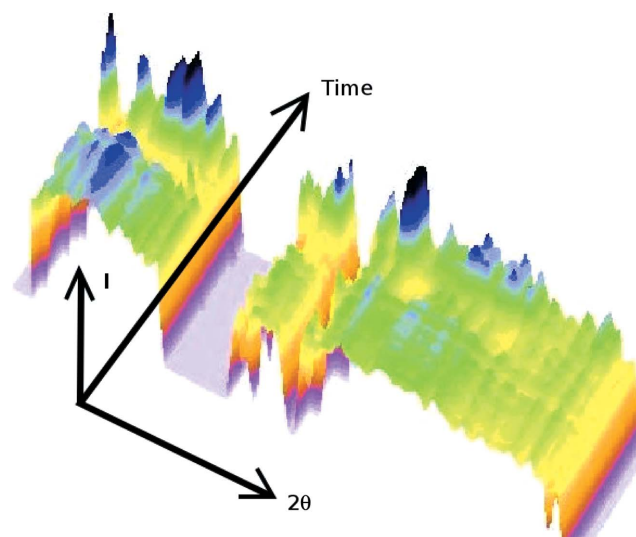

Figure 8
Crystallization of $CaO.2Al_2O_3$ from the liquid state. Radial distribution extracted from 20 ms frames recorded during the 4 s quench process. The hole is related to a chip that unfortunately was damaged at the time of the experiment.

recorded at 17 keV. The detector was located at 142 mm from the sample, corresponding to a pixel size of 0.13° and an angular aperture of 27°.

Data were processed according to expression (1) with a known flat field. The significant part of the reaction is plotted in Fig. 8 as a three-dimensional function of angle and time. Before the appearance of the low-temperature phase, the brief presence of another crystalline phase can be observed. Unfortunately the experiment was performed during a period in which chips were damaged, which accounts for the gap in the angular plot.

The design of a new experimental cell will improve counting statistics by at least a factor of four, thus allowing structural models involved in the crystallization process to be studied using the Rietveld method. The results reported here give rise to the following comments on kinetics experiments: count-rate considerations will limit these to a few milliseconds. Indeed, to be useful and have statistical meaning, a diffraction pattern must contain sufficient counts. It seems difficult to use a pattern with fewer than 1000 counts on the strongest lines, which corresponds to total rates of a few 10^6 counts s^{-1}. The advantage of the two-dimensional data collection is that this rate is handled by a line of pixels rather than by the single pixel of a linear detector. Thus, provided that the flux of the source is sufficient for each pixel to reach its highest counting rate, the real improvement is due to the number of pixels used.

5. Conclusions

This paper demonstrates that high-resolution data can be obtained with the XPAD photon-counting detector. Acquisition times can be reduced from 7 h, when using a conventional set-up with a point detector, to 0.5 h with XPAD. Further progress will be made with the next-generation XPAD3 by enabling tuning of all the pixels, and the time improvements

will be larger. Time-resolved experiments are now also possible with a dead-time between images of about 2 ms. With XPAD3, the whole time for image reading will remain 2 ms but its new design with buffered ouputs will allow the dead-time between images to be reduced to less than 1 µs, with acquisition times remaining larger than 2 ms. The new XPAD3 will be processed in 0.25 µm technology, thus allowing us to reduce the pixel size to 130 µm.

References

Basolo, S., Bérar, J.-F., Boudet, N., Breugnon, P., Caillot, B., Clemens, J.-C., Delpierre, P., Dinkespiller, B., Koudobine, I., Meessen, Ch., Menouni, M., Mouget, Ch., Pangaud, P., Potheau, R. & Vigeolas, E. (2005). *IEEE Trans. Nucl. Sci.* **52**, 1994–1998.

Bérar, J.-F., Blanquart, L., Boudet, N., Breugon, P., Caillot, B., Clemens, J.-C., Koudobine, I., Delpierre, P., Mouget, C., Potheau, R. & Valin, I. (2002*a*). *J. Phys. IV Fr.* **12**, 385–390.

Bérar, J.-F., Blanquart, L., Boudet, N., Breugon, P., Caillot, B., Clemens, J.-C., Koudobine, I., Delpierre, P., Mouget, C., Potheau, R. & Valin, I. (2002*b*). *J. Appl. Cryst.* **35**, 471–476.

Boudet, N., Bérar, J.-F., Blanquart, L., Breugon, P., Caillot, B., Clemens, J.-C., Koudobine, I., Delpierre, P., Mouget, C., Potheau, R. & Valin, I. (2003). *Nucl. Instrum. Methods A*, **510**, 41–44.

Brönnimann, Ch., Florin, S., Lindner, M., Schmitt, B. & Schulze-Briese, C. (2000). *J. Synchrotron Rad.* **7**, 301–306.

Delpierre, P., Bérar, J.-F., Blanquart, L., Boudet, N., Breugon, P., Caillot, B., Clemens, J.-C., Crest, L., Mouget, C., Potheau, R. & Valin, I. (2002). *IEEE Trans. Nucl. Sci.* **49**, 1709–1711.

Delpierre, P., Bérar, J.-F., Blanquart, L., Caillot, B., Clemens, J.-C. & Mouget, C. (2001). *IEEE Trans. Nucl. Sci.* **48**, 987–991.

Eikenberry, E. F., Barna, S. L., Tate, M. W., Rossi, G., Wixted, R. L., Sellin, P. J. & Gruner, S. M. (1998). *J. Synchrotron. Rad.* **5**, 252–255.

Hennet, L., Thiaudiere, D., Landron, C., Bérar, J.-F., Saboungi, M.-L., Matzen, G. & Price, D. L. (2003). *Nucl. Instrum. Methods Phys. Res. B*, **207**, 447–452.

Hennet, L., Thiaudiere, D., Landron, C., Melin, P., Price, D. L., Bérar, P., Coutures, J. P. & Saboungi, M.-L. (2003). *Appl. Phys. Lett.* **83**, 3305–3307.

Palancher, H. (2004). PhD thesis, University J. Fourier, Grenoble, France.

Palancher, H., Hodeau, J.-L., Pichon, C., Berar, J.-F., Lynch, J., Rebours, B. & Rodriguez-Carvajal, J. (2005). *Angew. Chem. Int. Ed.* **44**, 1725–1729.

Palancher, H., Pichon, C., Hodeau, J.-L., Berar, J.-F., Lynch, J., Rebours, B. & Rodriguez-Carvajal, J. (2006). *Z. Kristallogr.* **23**, 487–492.

Palancher, H., Pichon, C., Rebours, B., Hodeau, J.-L., Lynch, J., Berar, J.-F., Prevot, S., Conan, G. & Bouchard, C. (2005). *J. Appl. Cryst.* **38**, 370–373.

PSF (2006). *Python Software Fundation*, http://www.python.org/.

Rodriguez-Carvajal, J. (2001). *Commission on Powder Diffraction (IUCr) Newsletter*, No. 26, pp. 12–19. (http://www.fkf.mpg.de/cpd/cpd26.pdf).

Schlepütz, C. M., Herger, R., Willmott, P. R., Patterson, B. D., Bunk, O., Brönnimann, Ch., Henrich, B., Hülsen, G. & Eikenberry, E. F. (2005). *Acta Cryst.* A**61**, 418–425.

Watt, J., Bates, R., Campbell, M., Mathieson, K., Mikulec, B., O'Shea, V., Passmore, M. S., Schwarz, C., Smith, K. M. & Whitehill, C. (2001). *Nucl. Instrum. Methods Phys. Res. A*, **460**, 185–190.